MNRAS **000**, 1–15 (2019) Preprint 30 December 2021 Compiled using MNRAS LATEX style file v3.0

AstroSat view of MAXI J1535−571: broadband spectro-temporal features

Sreehari H.[1,5]*, Ravishankar B. T.[1,2], Nirmal Iyer[3], V. K. Agrawal[1], Tilak B. Katoch[4], Samir Mandal[2], Anuj Nandi[1]

[1]*Space Astronomy Group, ISITE Campus, U. R. Rao Satellite Centre, Outer Ring Road, Marathahalli, Bangalore, 560037, India*
[2]*Dept of Earth & Space Sciences, Indian Institute of Space Science and Technology, Thiruvananthapuram, 695547, India*
[3]*Albanova University Centre, KTH PAP, Stockholm, 10691, Sweden*
[4]*Department of Astronomy and Astrophysics, Tata Institute of Fundamental Research, Homi Bhabha Road, Colaba, Mumbai, 400005, India*
[5]*Department of Physics, Indian Institute of Science, Bangalore, 560012, India*

arXiv:1905.04656v1 [astro-ph.HE] 12 May 2019

Accepted 2019 May 10. Received 2019 May 10; in original form 2019 January 21

ABSTRACT

We present the results of Target of Opportunity (ToO) observations made with *AstroSat* of the newly discovered black hole binary MAXI J1535−571. We detect prominent C-type Quasi-periodic Oscillations (QPOs) of frequencies varying from 1.85 Hz to 2.88 Hz, along with distinct harmonics in all the *AstroSat* observations. We note that while the fundamental QPO is seen in the $3-50$ keV energy band, the harmonic is not significant above ~ 35 keV. The *AstroSat* observations were made in the hard intermediate state, as seen from state transitions observed by *MAXI* and *Swift*. We attempt spectral modelling of the broadband data ($0.7-80$ keV) provided by *AstroSat* using phenomenological and physical models. The spectral modelling using `nthComp` gives a photon index in the range between $2.18-2.37$ and electron temperature ranging from 21 to 63 keV. The seed photon temperature is within 0.19 to 0.29 keV. The high flux in $0.3-80$ keV band corresponds to a luminosity varying from 0.7 to 1.07 L_{Edd} assuming the source to be at a distance of 8 kpc and hosting a black hole with a mass of 6 $M_{\odot}$. The physical model based on the two-component accretion flow gives disc accretion rates as high as ~ 1 $\dot{m}_{Edd}$ and halo rate ~ 0.2 $\dot{m}_{Edd}$ respectively. The near Eddington accretion rate seems to be the main reason for the unprecedented high flux observed from this source. The two-component spectral fitting of *AstroSat* data also provides an estimate of a black hole mass between 5.14 to 7.83 $M_{\odot}$.

Key words: black hole physics – X-rays: binaries – stars: individual (MAXI J1535−571) – accretion

1 INTRODUCTION

X-ray binaries (XRBs) are astrophysical systems that are luminous in X-rays. An XRB hosts two stars of which one is either an accreting neutron star or black hole and the other is the mass donor which is referred to as the secondary star. XRBs are classified into low mass X-ray binaries (LMXBs) or high mass X-ray binaries (HMXBs) based on the mass of the secondary star (Seward & Charles 2010, and references therein). HMXBs tend to be persistently bright, whereas most of the LMXBs are transient in nature. LMXBs can remain in quiescence (below detection limit of the monitoring instruments) for a very long time and suddenly enter a transient phase exhibiting an outburst in the flux emitted. This increase in flux extends over a period of weeks to months, followed by a slower decay. Several hitherto unknown sources have been detected during such outbursts. Catalogs of black hole binaries discovered till 2016 can be found in Corral-Santana et al. (2016); Tetarenko et al. (2016). Prompt follow up observations, in different energy bands are required to understand the nature of the source and deduce the binary properties.

Emission from black hole binaries can be of thermal and non-thermal origins. The Keplerian accretion disc (Shakura & Sunyaev 1973) around a black hole is considered to be composed of concentric regions with different temperature, each radiating thermally and its total spectrum is approximated by a multi-

*E-mail: hjsreehari@gmail.com

© 2019 The Authors

color disk blackbody model (Mitsuda et al. 1984). Inverse-Comptonisation (Sunyaev & Titarchuk 1980; Titarchuk 1994; Tanaka & Lewin 1995) of the soft photons from the disc by a hot corona contributes to the higher energy thermal or non-thermal emission from the X-ray binary. The study of black hole binaries helps us to understand the nature of accretion processes in astrophysics. We can also infer the rate of mass accretion from the disc and corona in the source observed and understand their relative contributions to the flux. Spectral and temporal analysis gives astronomers an idea about the state evolution of the source during an outburst. Besides this, multi-wavelength observations are useful in studying the mechanism of outflows and jet ejection from these sources.

A plot of the hardness ratio versus the total flux is called the hardness intensity diagram (HID) (Homan et al. 2001) where hardness is the ratio of flux in hard band to that in soft band. It is generally observed that the HID of a complete outburst follows a 'q' profile (Homan & Belloni 2005; Nandi et al. 2012; Motta et al. 2012; Nandi et al. 2018; Radhika et al. 2018). Using HID and spectro-temporal parameters, one can classify the outburst periods of the black hole binaries into low hard state (LHS), hard intermediate state (HIMS), soft intermediate state (SIMS) and soft state (Homan et al. 2001; Homan & Belloni 2005; Remillard & McClintock 2006; Nandi et al. 2012).

Apart from the HID, the rms intensity diagram (RID) and the hardness rms diagram (HRD) (Motta et al. 2012; Belloni & Motta 2016) can also be used for state classification. Besides this, the presence of low frequency QPOs (LFQPOs) can indicate the state of a black hole binary system. C-type QPOs (Casella et al. 2005) are usually observed in LHS and HIMS whereas the presence of A and/or B-type QPOs correspond to SIMS (Radhika et al. 2016; Belloni & Motta 2016, and references therein).

The X-ray transient source MAXI J1535−571 was detected independently by *MAXI* (Monitor of All-sky X-ray Image) and *Swift/BAT* on Sep 2, 2017 (Negoro et al. (2017a) and Kennea et al. (2017)) at (RA, DEC) = (15 35 19.73, −57 13 48.1). Negoro et al. (2017b) suggested that it could be a black hole LMXB, based on the observed rapid random X-ray variability and column density. The unprecedented large flux levels prompted a flurry of observations made by different observatories as detailed below. A strong radio counterpart was detected using *ATCA* data with spectral `powerlaw` index of 0.09 ± 0.03. This suggested emission from a compact radio jet (Russell et al. 2017a). *Swift/XRT* data in the rising phase of the outburst revealed C-type QPOs at 4.00 ± 0.05 Hz, 3.67 ± 0.05 Hz and 2.50 ± 0.02 Hz (Russell et al. 2017b), and evolution of QPOs from 0.21 ± 0.03 Hz to 3.22 ± 0.04 Hz (Mereminskiy & Grebenev 2017; Mereminskiy et al. 2018) using *Swift* and *INTEGRAL* data. Shang et al. (2018) also observed QPOs in the range between 0.44 to 6.48 Hz using *Swift/XRT* data in the period MJD 58004 to 58050. *MAXI* and *Swift* monitoring of the outburst as it reached its peak in about 20 days since detection showed state changes (Nakahira et al. 2017; Kennea 2017; Shidatsu et al. 2017). Negoro et al. (2018a) reported that the source flux dropped sharply by MJD 58200 (by Mar 23, 2018) below detection limit in *MAXI*, while the source was in the soft state. X-ray and Radio detections with state changes were nevertheless reported beyond this too (Russell et al. 2018a,b; Parikh et al. 2018; Negoro et al. 2018b).

Nakahira et al. (2018) provided the details of monitoring with *MAXI* $2 - 20$ keV energy band, and the state changes till fading of the source. Xu et al. (2018) described the *NuSTAR* spectra considering the disc reflection features while modelling the broad Fe-K line and Compton hump in $20 - 50$ keV. They deduced a black hole spin $a > 0.84$, inner disc radius $R_{in} < 2.01\ r_{ISCO}$, and a lamp-post height $h = 7.2^{+0.8}_{-2.0}\ r_{\rm g}$ for a compact coronal illuminating source. Tao et al. (2018) made use of the *XRT* data from the entire outburst phase to examine the hardness based state changes, and evolution of spectral properties. Baglio et al. (2018) discussed about the possibility of using rapid variability in mid-IR in order to study the disc-jet connection. Recently, Stiele & Kong (2018) have done detailed timing and spectral analysis of this source using data from *XRT*, *XMM-Newton* and *NICER* observatories. Also, Stevens et al. (2018) detected LFQPO of $5.72^{+0.04}_{-0.06}$ Hz in the average power spectrum corresponding to the *NICER* observations from MJD 58016 to 58026, when the source was in SIMS. Huang et al. (2018) reported on timing and spectral analysis using data from *HXMT* and suggested that MAXI J1535−571 could be a high inclination system. Analysis of *NICER* spectrum in the energy range $2.3 - 10$ keV by Miller et al. (2018) also indicated a high inclination of $67.4 \pm 0.8^{\circ}$. Besides this, Miller et al. (2018) determined that the source spins at near maximal rate of 0.994 ± 0.002. Though there are estimates on the inclination and spin of the system, the distance and mass of the black hole are yet to be estimated. In this work, we have used our physical model to estimate the mass of MAXI J1535−571.

AstroSat ToO observations were triggered on MAXI J1535−571, in the second week after its detection. *AstroSat* is India's first satellite, dedicated to astronomy. The broadband coverage and high sensitivity of *LAXPC* and *SXT* onboard *AstroSat*, enabled simultaneous spectral and temporal studies of the source. We studied the nature and energy dependence of LFQPOs and the broadband spectrum using these observations. We modelled the broadband spectrum in the energy range $0.7 - 80$ keV phenomenologically as well as in the framework of the two-component accretion flow (Chakrabarti & Titarchuk 1995; Chakrabarti & Mandal 2006; Iyer et al. 2015). This allowed us to compute the accretion rates for the source and also to estimate the mass of the black hole. In order to augment the 6 days of *AstroSat* observations, we also used data from observations with *Swift/XRT* and *MAXI*.

In §2, we have given details on the observation and steps for data reduction. We have discussed the outburst profile and HID of this outburst in §3. Detailed temporal analysis was done with *AstroSat/LAXPC* and the results are presented in §4. We undertook a broadband spectral analysis using both *SXT* and *LAXPC* data and the results from phenomenological as well as physical modelling are presented in §5. Finally, we have discussed the results and have concluded in §6.

2 OBSERVATION AND DATA REDUCTION

AstroSat provides a unique platform for simultaneous obser-

vations, over a wide X-ray band from 0.3 keV to 100 keV, via its suite of co-aligned X-ray instruments – Soft X-ray Telescope (*SXT*) (Singh et al. 2016, 2017), Large Area X-ray Proportional Counter (*LAXPC*) (Yadav et al. 2016b; Antia et al. 2017) and Cadmium Zinc Telluride Imager (*CZTI*) (Vadawale et al. 2016). We exploit the detection capabilities of *SXT* in the soft X-rays to obtain spectra in the lower energies and *LAXPC* enables us to study spectra upto 80 keV. We also make use of the temporal resolution (10 μs) of *LAXPC* to search for QPOs across a wide range of frequencies.

The ToO observations of *AstroSat* were scheduled over 62 slots, each of about a few ks exposure (Table A1), intermittently between Sep 12, 2017 (MJD 58008.23) till Sep 17, 2017 (MJD 58013.15). These were the days when the source was reported by monitoring observations to be softening compared to the initial hard state though the spectrum below 10 keV remained non-thermal (Nakahira et al. 2017; Kennea 2017; Palmer et al. 2017). We made use of data from *SXT* and *LAXPC*, which operate respectively in 0.3 keV to 8 keV and 3 keV to 80 keV bands, for the timing and spectral analyses. The *AstroSat* level 1 ToO data were obtained from the ISSDC data dissemination archive[1]. Table A1 lists details of all the *AstroSat* observations of MAXI J1535−571, including orbit numbers and exposure time.

The *Swift* mission, as mentioned earlier, continuously monitored the source from its first detection of the outburst. We made use of the *XRT* data in the 0.3 keV to 10 keV band, in order to augment the *AstroSat* data used in the analysis. The *XRT* data were obtained from the HEASARC public archive[2]. Details of all publicly available *Swift* monitoring data are provided in Table B1.

We also used data from *MAXI*[3] to plot the outburst flux profile and the HID. Besides these X-ray instruments, we used radio results from the Australia Telescope Compact Array (*ATCA*) and Atacama Large Millimeter/submillimeter Array (*ALMA*) to study the radio flux levels during the outburst. Note that the radio results used are the ones available in Russell et al. (2017a,b); Tetarenko et al. (2017). There are more observations reported by ALMA (Russell et al. 2018a). However, those results are not yet published.

2.1 *AstroSat* Data Reduction

Firstly, we carried out temporal and spectral analysis of the source MAXI J1535−571 using *AstroSat* data. The capabilities of *LAXPC* for timing and spectroscopic studies of various sources are already demonstrated by Yadav et al. (2016a); Misra et al. (2017); Verdhan Chauhan et al. (2017). We followed these papers and the instructions[4] provided along with the *LAXPC* analysis software (`LaxpcSoft`[5]) released on May 19, 2018. The details of how the responses and background spectra are generated are given by Antia et al. (2017).

The three *LAXPC* detectors (*LAXPC10, LAXPC20* and *LAXPC30*) were operated in the normal or Event Analysis (EA) mode, in all those observations between Sep 12 – Sep 17, 2017. Of the 62 sets of data in Table A1, we used 15 for our analysis, sampling a few from the several orbits of observation per day. Selected orbit numbers have been bold-faced in the table. As will be evident from the results in §4 and §5, the temporal and spectral parameters do not evolve indicating that the selected observations are enough to characterise the source.

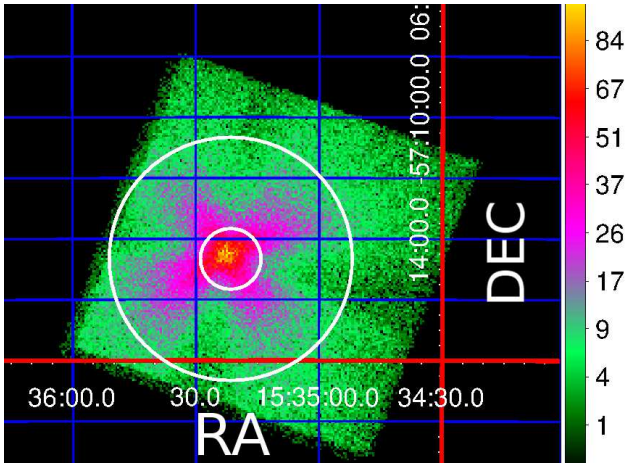


Figure 1. Image of the source MAXI J1535−571 taken on MJD 58009.55 using the *SXT* instrument aboard *AstroSat*. In order to address the pile-up issue in the *SXT* Fast Windowed mode data, we have selected the source region as an annulus with inner and outer radii 1′ and 4′ respectively, as shown. The colourmap alongside is for the source intensity in *SXT* cts pixel^{-1}.

Of the three *LAXPC* detectors, data from *LAXPC10*, and in that, the eventlist subset corresponding to the longest available good time interval slot has been used for analysis. The lightcurve has been extracted in the 3 − 80 keV energy range with a resolution of 0.005 s which corresponds to power spectra ranging upto a frequency of 100 Hz. The background subtracted mean count rate for the *LAXPC10* observations varied from around 4400 cts/s to 6300 cts/s. We also generated lightcurves in the energy bands 3 − 20 keV, 20−35 keV, 35−50 keV and 50−80 keV for selected observations to study the energy dependent evolution of the features in the power spectrum. Further, the source and background energy spectra were generated. Out of the three layers of *LAXPC*, we used data from the top layer only. Moreover, only single events were considered for generating the spectra. These options were selected to have a minimal undesired bump in the spectral residuals at around 33 keV. A systematic error of 2% has been added while creating the background spectrum. `XSPEC v 12.9.1` has been used for spectral analysis and modelling.

SXT is an instrument capable of X-ray imaging and spectroscopy in the 0.3 − 8 keV energy range. *SXT* has a focusing telescope and a CCD detector (Singh et al. 2017). Extraction of level 2 data from *SXT* has been done using the `sxtpipeline` tool. The *SXT* data are available in the Fast Windowed (FW) mode. The extracted cleaned event file is used to generate energy spectra with `XSELECT V2.4d`. The image count rate at the central pixels goes as high as 369 cts/s which crosses the pile-up limit of 344 cts/s for FW

[1] https://gads.issdc.gov.in/astro-gads/
[2] https://heasarc.gsfc.nasa.gov/cgi-bin/W3Browse/w3browse.pl
[3] http://maxi.riken.jp/mxondem/
[4] http://astrosat-ssc.iucaa.in/?q=laxpcData
[5] http://www.tifr.res.in/∼astrosat_laxpc/LaxpcSoft.html

mode as indicated in the *AstroSat Handbook*[6]. To avoid pile-up effects, an annular region centred at the source RA and DEC, and of $1'$ inner radius and $4'$ outer radius is chosen to extract the spectrum. In Figure 1, we have shown an example of choosing source region excluding the central $1'$ from *SXT* data. It is evident from the figure that the largest radius for the annulus possible in this mode is $4'$. The average count rate of the entire image is 175 cts/s and it reduces to 101 cts/s after filtering the region using the annulus as mentioned above. We used the background, response and ARF files provided by the *SXT* instrument team[7] for the analysis.

2.2 *Swift/XRT* Data Reduction

Among all the *Swift* observations of the source in the public archive, the ones that we selected for analysis are indicated by bold-faced ObsIds in Table B1. All *XRT* observations from 02 Sep 2017 to 10 Mar 2018 with an exposure greater than 800 s were considered for this analysis. For temporal analysis, lightcurves, power spectra and hardness ratios of all datasets were obtained. *XRT* data extraction was done using steps outlined in the *XRT* reduction manual[8]. `HEAsoft v 6.21` was used to reduce the data with CALDB updated till Jan 2018. All *XRT* data used were taken in the Windowed Timing (WT) mode. Initial reduction was done using the ftool `xrtpipeline` with event grades between $0-2$ chosen. The cleaned event files so obtained were used for further analysis.

For generating the power spectra, lightcurves with a bin size of 0.005 s were made using photons in the energy range $0.5-10$ keV and $3-10$ keV (for compatibility with *AstroSat* results). All observations with an average count rate >100 cts/s were treated for pile-up effects. We selected the source extraction region using an annulus of inner radius $12.5''$ and outer radius $50''$, centred on the source position. Data from the region within the inner radius of the annulus was discarded to correct for pile-up. The power spectra were generated from these pile-up corrected lightcurves as explained in §4.2. Lightcurves with a time bin of 1 s in the bands $0.5-4$ keV and $4-10$ keV were created to compute the hardness ratio between these bands. In the next section, we present the outburst profile and HID.

3 2017 OUTBURST PROFILE AND HARDNESS INTENSITY

Figure 2 shows the *MAXI* outburst profile in $2-20$ keV, *XRT* light curve ($0.3-10$ keV), radio detections made using *ATCA* & *ALMA*, *MAXI* HR1 ($4-10$ keV / $2-4$ keV) and *MAXI* HR2 ($10-20$ keV / $4-10$ keV), respectively, from top to bottom. MJDs corresponding to *AstroSat* observations are shaded in all the panels. It can be noticed that the *MAXI* and *XRT* flux vary similarly. Radio flux of the order of a few hundred mJy was observed just before the observations by *AstroSat*. It is to be noted that the radio activity observed in black hole binaries are strongly correlated with spectral states (Radhika et al. 2016), and thus the radio results confirm that MAXI J1535−571 was making a transition to HIMS in that period. HR1 decreased from a high value of around 1.0 at the beginning of the outburst to below 0.1 as the flux reduced considerably. Meanwhile HR2 remained low throughout the outburst except during the initial few days.

Figure 3 shows the Hardness Intensity Diagram (HID) produced from the same *MAXI* data points used in Figure 2. The hardness ratio ($6-20$ keV / $2-6$ keV) is plotted against MAXI $2-20$ keV band flux. The uncertainty on the *MAXI* flux increased as the outburst activity dropped beyond MJD $\sim$ 58100 and that in turn caused the significant spread in the HID regime of flux $\leq$ 2 ph cm^{-2} s^{-1} and hardness $\leq$ 0.1. The *LAXPC* observations were made just before the outburst peak, when the source was in HIMS with a hardness around 0.3. In this figure, LHS is represented by red circles, HIMS by golden filled circles, SIMS by turquoise filled inverted triangles, and soft state is represented using cyan triangles. The states are marked as per the classification done by Tao et al. (2018).

The blue shaded region representing *AstroSat* observations, falls in HIMS of the outburst. Beyond the HIMS, the source hardness decreased as can be seen from Figure 3. In this phase starting from MJD 58015, the source entered SIMS (Huang et al. 2018). The HID for this source does not follow the exact 'q' - shape that is exhibited by canonical black hole binaries (Belloni et al. 2005; Nandi et al. 2012; Radhika et al. 2018). Instead, we noticed an increase in hardness ratio after the source reached its peak indicating a transition back to the HIMS. This continued for a few days (MJD 58049 to 58051) before the hardness ratio started decreasing again. Though there is no XRT observation following this until MJD 58137, the decrease in hardness ratio from *MAXI* HID indicates that the source had gone back to SIMS in this period. After that, both flux and hardness ratios decreased considerably. Tao et al. (2018) have classified this period as soft state (from MJD 58137 to 58230). In §4 we present the procedure and results of temporal analysis of this outburst.

4 TIMING ANALYSIS AND RESULTS

4.1 Timing Analysis

Initially, we generated 1 s lightcurves from *LAXPC* and obtained the count rates corresponding to each observation. We did not observe any signature of structured variability in these lightcurves. Then we created 0.005 s resolution lightcurves from *LAXPC10* data sets to generate the power spectra. We divided each lightcurve in the intervals of 8192 time bins, and then created power density spectra (hereafter PDS) for each interval. The final PDS for each lightcurve was generated after averaging these individual PDS. The averaged PDS was binned by a factor of 1.05 in frequency space. We have fitted the PDS with the combination of 4 `Lorentzians` representing a broad band limited noise (BLN; a zero centered `Lorentzian`), a low frequency noise (LFN), QPO and its upper harmonics. We took the QPO frequency as the centroid of the `Lorentzian` component fitting the QPO. QPOs were identified by fitting a multi-Lorentzian model to the entire power spectrum and

[6] http://www.iucaa.in/~astrosat/AstroSat_handbook.pdf
[7] http://www.tifr.res.in/~astrosat_sxt/dataanalysis.html
[8] https://swift.gsfc.nasa.gov/analysis/xrt_swguide_v1_2.pdf

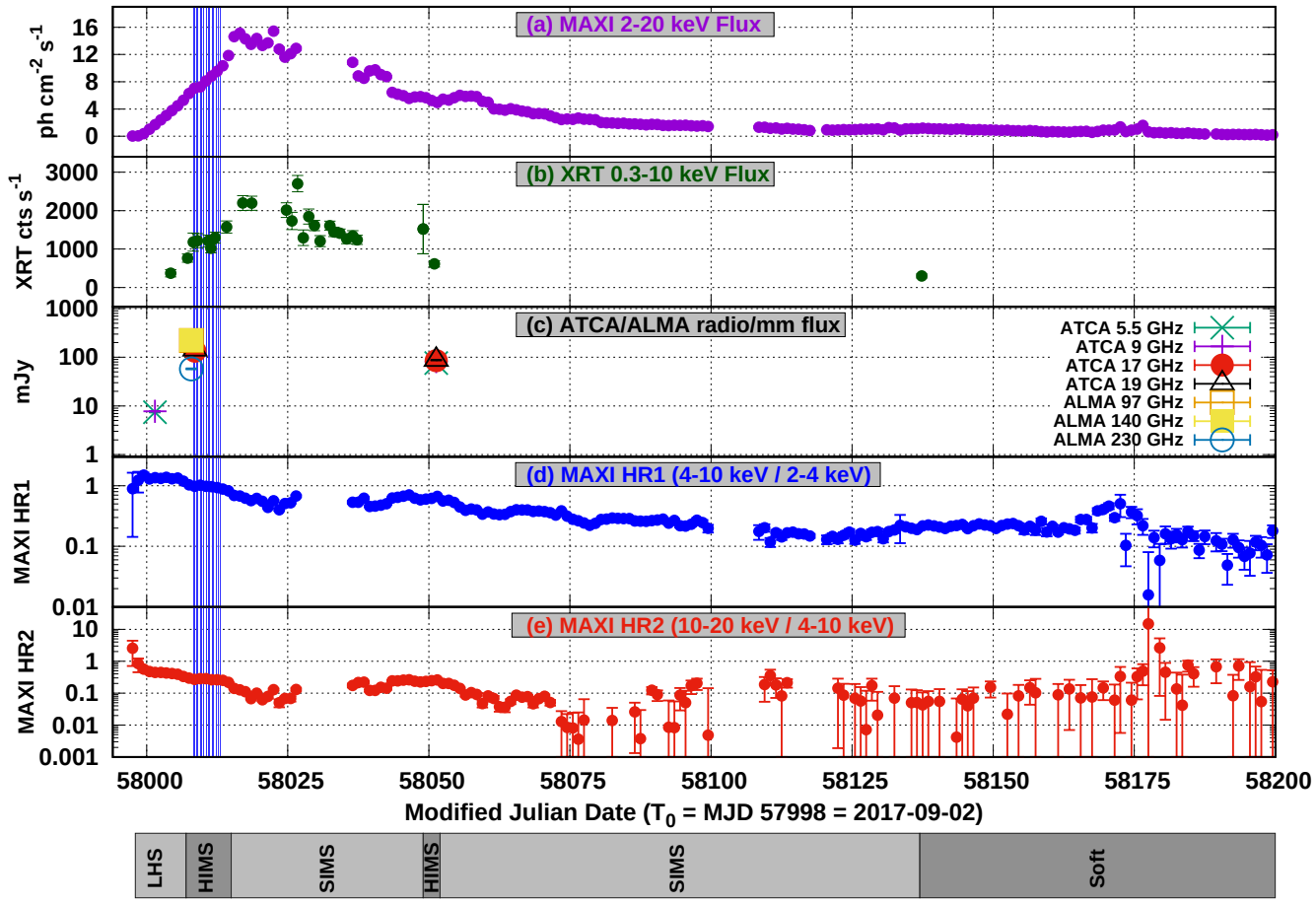


Figure 2. *AstroSat* observation slots between Sep 12 till Sep 17, 2017 indicated as vertical blue bars in all panels. (a) *MAXI* $2-20$ keV light curve of the outburst; (b) *XRT* $0.3-10$ keV light curve; (c) *ATCA/ALMA* radio detections of the source (observations reported in Russell et al. (2018a) are not included); (d) *MAXI* HR1 ($4-10$ keV / $2-4$ keV); and (e) *MAXI* HR2 ($10-20$ keV / $4-10$ keV). Indicated at the bottom is the sequence of different spectral states of the system during the evolution of the outburst, as determined in this work, and also commensurate with Tao et al. (2018).

searching for features with *quality factor*, $Q = \frac{\nu}{\Delta\nu} > 3$ and $Significance = \frac{Norm}{Err_{norm}} > 3$, where ν is `Lorentzian` centroid frequency, $\Delta\nu$ is FWHM and Err_{norm} is the negative error in norm.

Further, we subtracted the dead-time (τ_d) affected Poisson noise level (Agrawal et al. 2018). Besides altering the noise level, the dead-time effects can also change the source rms (van der Klis 1989). Therefore, we applied correction on rms as prescribed by Bachetti et al. (2015) to account for the effect of dead-time. The dead-time corrected rms (rms_{in}) is calculated as $rms_{in} = rms_{det}/(1 - \tau_d\, r_{det})$, where rms_{det} is the detected rms and r_{det} is the detected count rate. We modelled the resultant PDS in frequency-rms space using multiple `Lorentzians` as mentioned before. The QPO rms amplitude in percentage was computed by finding the area under the `Lorentzian` corresponding to the QPO, in the frequency range between 0.05 to 100 Hz. RMS calculations were done for the full band ($3-80$ keV) as well as for the $3-10$ keV using *LAXPC10* data in the $0.05-100$ Hz frequency range. Similarly, we computed rms for the *XRT* data in the range $0.5-10$ keV as well as for the $3-10$ keV band in order to compare with *LAXPC10* results. Total rms of each PDS was obtained by adding the rms of individual features in quadrature.

Figure 4 shows the power spectrum corresponding to the observation on MJD 58008.24. This was obtained from a lightcurve in the range $3-80$ keV. The power spectrum in frequency-rms space was modelled with multiple `Lorentzians` corresponding to fundamental QPO , its harmonic, BLN and LFN. The fundamental frequency was found to be 2.21 ± 0.02 Hz with an FWHM of 0.24 ± 0.02 Hz. The second harmonic was found at 4.37 ± 0.03 Hz with an FWHM of 0.76 ± 0.10 Hz. The percentage rms of the fundamental frequency was 8.23 ± 0.49 and for the second harmonic, it was 4.10 ± 0.37. The BLN contributed $11.30\pm1.44\%$ rms and the LFN had rms of $6.56\pm1.02\%$. The χ^2/dof for this fit was 0.98 (115.7/118). Unless mentioned explicitly, all the errors are computed using $\Delta\chi^2 = 1.0$ (68% confidence level) for all the observations (see Tables 1 and 2). The detection of a QPO and its harmonic in this PDS encouraged us to do an energy dependent analysis of the power spectra, and the details are presented in §4.3.

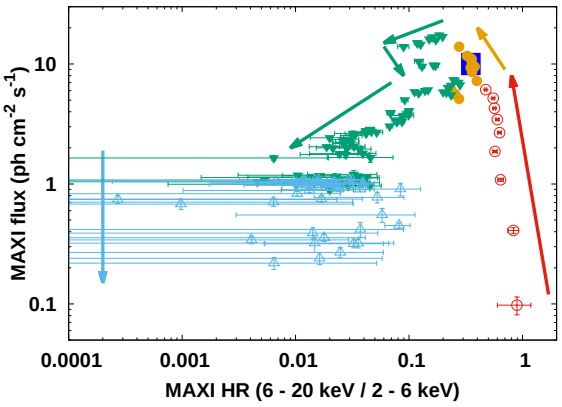


Figure 3. MAXI Hardness-Intensity Diagram (HID) showing evolution of the hardness ratio ($6-20$ keV / $2-6$ keV) with the MAXI $2-20$ keV Flux. Here LHS is represented by red circles, HIMS by golden filled circles, SIMS by turquoise filled inverted triangles, and soft state is represented using cyan triangles. Times corresponding to *AstroSat/LAXPC* observations are shown as a blue patch. The arrows indicate the direction in which the outburst evolves with time.

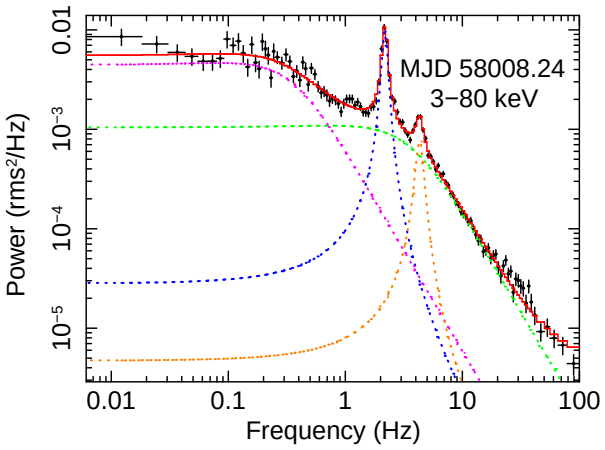


Figure 4. Power spectrum of MAXI J1535−571 for the energy band $3-80$ keV corresponding to the *LAXPC* observation on MJD 58008.24 (Orbit 10585) fitted with multiple `Lorentzians`. A QPO at 2.21 ± 0.02 Hz and its harmonic are evident in the PDS. We have also plotted the unfolded model to show the relative contributions of the model components.

4.2 Relation between flux and RMS

We generated the power spectra from *XRT* lightcurves (pile-up corrected) in the $0.5-10$ keV energy range, using the ftool `powspec`, considering 8192 bins per interval. The deadtime correction factor for *XRT* is ~ 1 and so it does not affect the power spectrum. Exposure correction was not applied as it can affect the Poissonian nature of the noise power. The power spectrum in frequency-rms space was integrated from 0.05 to 100 Hz to compute the rms value. The evolution of fractional rms variability of the *XRT* observations with respect to hardness and intensity is shown in Figure 5. Hardness was calculated as the ratio of flux in $4-10$ keV to the flux in $0.5-4$ keV. Total rms for each PDS was calculated using the `imodel` command of QDP[9]. Here hollow circles represent LHS, filled circles represent HIMS, inverted triangles stand for SIMS and hollow triangles indicate soft state. The arrows have colours assigned as in Figure 3 based on the state at the tail of the arrow. Motta et al. (2012); Belloni & Motta (2016) show the general trend of an HRD corresponding to a canonical black hole binary outburst where the rms during LHS varies from $\sim$ 20 to 40%, HIMS from $\sim$ 10 to 20% and below $\sim$ 5% in the softer states. Figure 5a shows the HRD for MAXI J1535−571 with *XRT* data from which it was evident that at the beginning of the outburst in LHS, the hardness (0.56) and rms (around 35%) are both at a comparatively larger value. In the HIMS, the rms value was observed to be in the range 10 to 20%. As the outburst progressed, the rms value decreased to around 6% in SIMS. *AstroSat* observations are indicated by the blue shaded portion. These observations were made just before the drop in rms values. The observation from soft state shown in the HRD has a significantly high value of rms ($\sim$ 17%) as compared to other sources (see Nandi et al. 2012; Motta et al. 2012; Radhika et al. 2018).

From Figure 5b, we can see that in the LHS, though the source had highest rms ($\sim$ 35%), the flux was below $\sim$ 400 cts/s. In HIMS, we observe count rates in between 600 and 1500 cts/s and rms within $\sim$ 10 to 25%. RID for other sources (Muñoz-Darias et al. 2011) also have higher count rates in the intermediate states as compared to the hard state. The rms and hardness of the *AstroSat* observation period suggests that the source was in HIMS as indicated by the golden arrows and filled circles. This is consistent with the spectral state classification by Tao et al. (2018). The RID shows dip in rms values in the SIMS. Besides this, the intensity peaks (above 2000 cts/s) during the time when the rms has lowest values ($\sim$ 6%).

4.3 Temporal Properties

As detailed above, we modelled all the 15 *LAXPC* power spectra with multiple `Lorentzians` and it was observed that the frequency of the fundamental QPO varies from 1.85 Hz to 2.88 Hz. The quality factor (Q) for the QPOs are around 9.0 and the significance was also high ($\sim$ 10.0). The QPO rms amplitude was near 8.5% for all the *LAXPC* observations. The harmonics have Q-factor around 5.0, significance around 10.0 and rms varying from 3.68 to 4.85%. Low frequency noise (LFN) with rms around 6.5% and band limited noise (BLN) with rms around 10% are also present in the power spectra. These QPO parameters are tabulated in Table 1. There was no indication of increase/decrease of fundamental frequency with time. Based on Casella et al. (2005); Belloni & Motta (2016), we have classified the QPOs as C-type as they are in the frequency range from $\sim 2-3$ Hz, have $Q \sim 9$ and rms of around 8.5%, and appear along with strong band limited flat noise component. The strong QPOs observed in this source could be possibly due to the oscillation of post-shock corona (hereafter PSC; see Das et al. 2014).

Figure 6 consists of the energy dependent Power Density Spectra (PDS) obtained with *AstroSat/LAXPC* for the

[9] https://heasarc.gsfc.nasa.gov/ftools/others/qdp/qdp.html

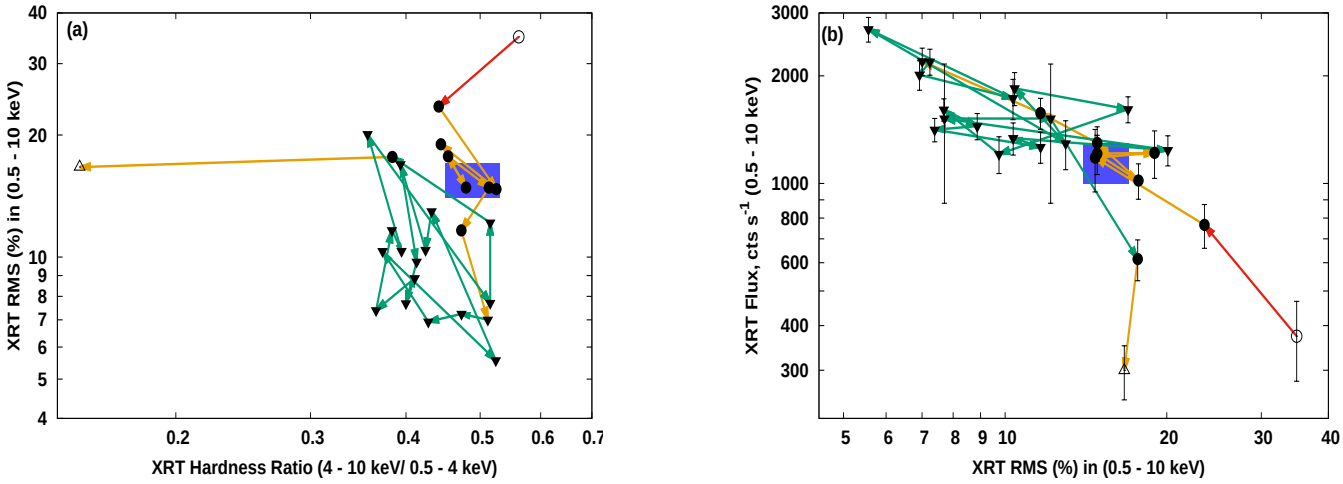


Figure 5. (a) XRT Hardness-RMS Diagram (HRD) and on panel (b) we have the RMS Intensity Diagram (RID). Here hollow circles represent LHS, filled circles represent HIMS, inverted triangles stand for SIMS and hollow triangles indicate soft state. The arrow colours have same meaning as in Figure 3. Also, times corresponding to *LAXPC* observations are shown as blue patches.

Table 1. QPO parameters for the 15 orbits data of *AstroSat/LAXPC* in the full energy band of 3 − 80 keV. These results are from modelling the power spectrum after dead time correction and Poisson noise subtraction.

MJD	Orbit	Mean rate (cts/s)	QPO (Hz)	Q-factor	Sig^b (σ)	amplitude (rms %)	Harmonic (Hz)	Q-factor	Sig^b (σ)	amplitude (rms %)	BLN (rms %)	LFN (rms %)	red. χ^2 (χ^2/dof)
58008.24	10585	4479	2.21 ± 0.02	9.20	11.78	8.23 ± 0.49	4.37 ± 0.03	5.75	10.30	4.10 ± 0.37	11.3 ± 1.44	6.56 ± 1.02	0.98 (115.7/118)
58008.53	10589	5337	2.65 ± 0.01	8.54	13.76	8.51 ± 0.41	5.24 ± 0.04	5.88	10.63	3.68 ± 0.29	10.7 ± 1.25	7.03 ± 0.69	0.99 (116.7/118)
58008.82	10594	5398	2.54 ± 0.01	8.75	09.22	8.42 ± 0.63	4.95 ± 0.05	4.54	07.75	4.32 ± 0.63	9.83 ± 2.03	7.37 ± 0.96	0.89 (105.1/118)
58009.02	10597	5618	2.88 ± 0.01	10.28	14.10	8.56 ± 0.42	5.68 ± 0.04	4.89	10.69	4.00 ± 0.39	9.91 ± 1.22	7.29 ± 0.64	1.39 (164.0/118)
58009.55	10604	5593	2.56 ± 0.01	9.48	09.89	8.46 ± 0.66	5.02 ± 0.04	4.29	08.38	4.28 ± 0.53	10.0 ± 1.63	6.86 ± 1.03	1.70 (200.3/118)
58009.77	10608	5590	2.02 ± 0.02	8.41	07.58	8.44 ± 0.80	3.99 ± 0.06	3.21	07.30	4.85 ± 0.90	9.99 ± 2.24	6.50 ± 1.33	0.93 (110.0/118)
58010.03	10612	5642	1.85 ± 0.01	9.73	12.53	8.22 ± 0.46	3.72 ± 0.03	4.76	10.92	4.53 ± 0.39	11.2 ± 1.76	6.14 ± 1.48	0.83 (98.0/118)
58010.49	10618	5708	2.08 ± 0.01	11.55	09.87	8.42 ± 0.64	4.15 ± 0.03	5.60	10.09	4.39 ± 0.40	11.2 ± 1.35	6.23 ± 1.08	1.09 (128.6/118)
58010.92	10625	5910	2.20 ± 0.01	9.56	11.38	8.35 ± 0.42	4.33 ± 0.03	5.85	09.08	4.17 ± 0.46	10.8 ± 1.61	6.61 ± 1.17	0.91 (107.3/118)
58011.13	10628	5923	2.17 ± 0.01	9.43	13.71	8.44 ± 0.48	4.30 ± 0.02	7.16	11.80	3.87 ± 0.28	11.1 ± 1.08	6.61 ± 0.72	1.15 (135.2/118)
58011.66	10636	6011	2.31 ± 0.01	9.62	08.61	8.73 ± 0.77	4.53 ± 0.03	7.07	07.27	3.85 ± 0.48	10.4 ± 2.12	6.80 ± 1.31	0.68 (80.8/118)
58011.87	10639	6035	2.21 ± 0.01	9.60	09.85	8.62 ± 0.56	4.38 ± 0.03	6.53	08.39	3.95 ± 0.45	10.5 ± 1.76	6.87 ± 1.12	0.78 (92.3/118)
58012.24	10644	6189	2.59 ± 0.01	8.63	15.52	8.86 ± 0.42	5.09 ± 0.03	5.19	13.88	3.94 ± 0.31	9.93 ± 1.53	8.03 ± 0.73	1.66 (197.6/119)
58012.67	10651	6282	2.46 ± 0.02	9.11	08.88	8.82 ± 0.69	4.83 ± 0.04	5.81	07.51	3.98 ± 0.49	9.56 ± 2.25	7.21 ± 1.26	0.69 (81.0/118)
58013.02	10656	6338	2.11 ± 0.01	9.59	10.04	8.89 ± 0.58	4.20 ± 0.03	4.82	11.83	4.46 ± 0.49	10.1 ± 2.34	7.45 ± 1.17	1.35 (159.4/118)

[b] Significance

Table 2. Energy dependent QPO parameters of MAXI J1535−571 from *AstroSat/LAXPC*. Power spectra have been modelled in frequency-rms space. The parameters corresponding to the fundamental component are indicated with (f) and those corresponding to the harmonic component with (h).

MJD	E-band keV	QPO(f) Hz	FWHM(f) Hz	Norm(f)	Q(f)	sig(f)^a (σ)	rms(f) (%)	QPO(h) Hz	FWHM(h) Hz	Norm(h)	Q(h)	sig(h)^a (σ)	rms(h) (%)
	3 – 20	2.22 ± 0.01	0.23 ± 0.02	0.018	9.64	11.05	8.09 ± 0.46	4.43 ± 0.03	0.60 ± 0.08	0.0018	7.38	9.84	5.09 ± 0.42
58008.24	20 – 35	2.19 ± 0.01	0.21 ± 0.03	0.021	10.42	7.95	8.44 ± 0.82	$4.57^{+0.14}_{-0.10}$	$0.78^{+0.62}_{-0.34}$	0.0018	5.85	3.53	4.71 ± 1.62
	35 – 50	$2.22^{+0.07}_{-0.05}$	$0.31^{+0.12}_{-0.16}$	0.010	7.16	4.47	7.12 ± 2.53	-	-	-	-	-	
	50 – 80	-	-	-	-	-	-	-	-	-	-	-	
	3 – 20	2.89 ± 0.01	0.29 ± 0.02	0.016	9.96	11.78	8.61 ± 0.45	5.72 ± 0.03	$0.87^{+0.11}_{-0.09}$	0.0013	6.57	12.76	4.17 ± 0.36
58009.02	20 – 35	2.88 ± 0.01	0.22 ± 0.02	0.023	13.09	9.91	9.09 ± 0.69	$5.86^{+0.10}_{-0.09}$	$0.82^{+0.50}_{-0.32}$	0.0019	7.14	4.08	5.02 ± 1.43
	35 – 50	2.87 ± 0.03	$0.19^{+0.06}_{-0.09}$	0.014	15.10	4.28	6.61 ± 2.20	-	-	-	-	-	
	50 – 80	-	-	-	-	-	-	-	-	-	-	-	
	3 – 20	2.61 ± 0.01	0.28 ± 0.01	0.016	9.32	15.18	8.58 ± 0.35	5.14 ± 0.02	$0.84^{+0.11}_{-0.09}$	0.0013	6.11	13.82	4.19 ± 0.29
58012.24	20 – 35	2.59 ± 0.01	0.26 ± 0.02	0.020	9.96	11.30	9.27 ± 0.57	5.35 ± 0.10	$1.09^{+0.45}_{-0.30}$	0.0016	4.90	5.16	5.24 ± 1.05
	35 – 50	$2.58^{+0.04}_{-0.06}$	$0.24^{+0.07}_{-0.21}$	0.0099	10.75	4.75	6.14 ± 1.93	-	-	-	-	-	
	50 – 80	-	-	-	-	-	-	-	-	-	-	-	

[a] Significance

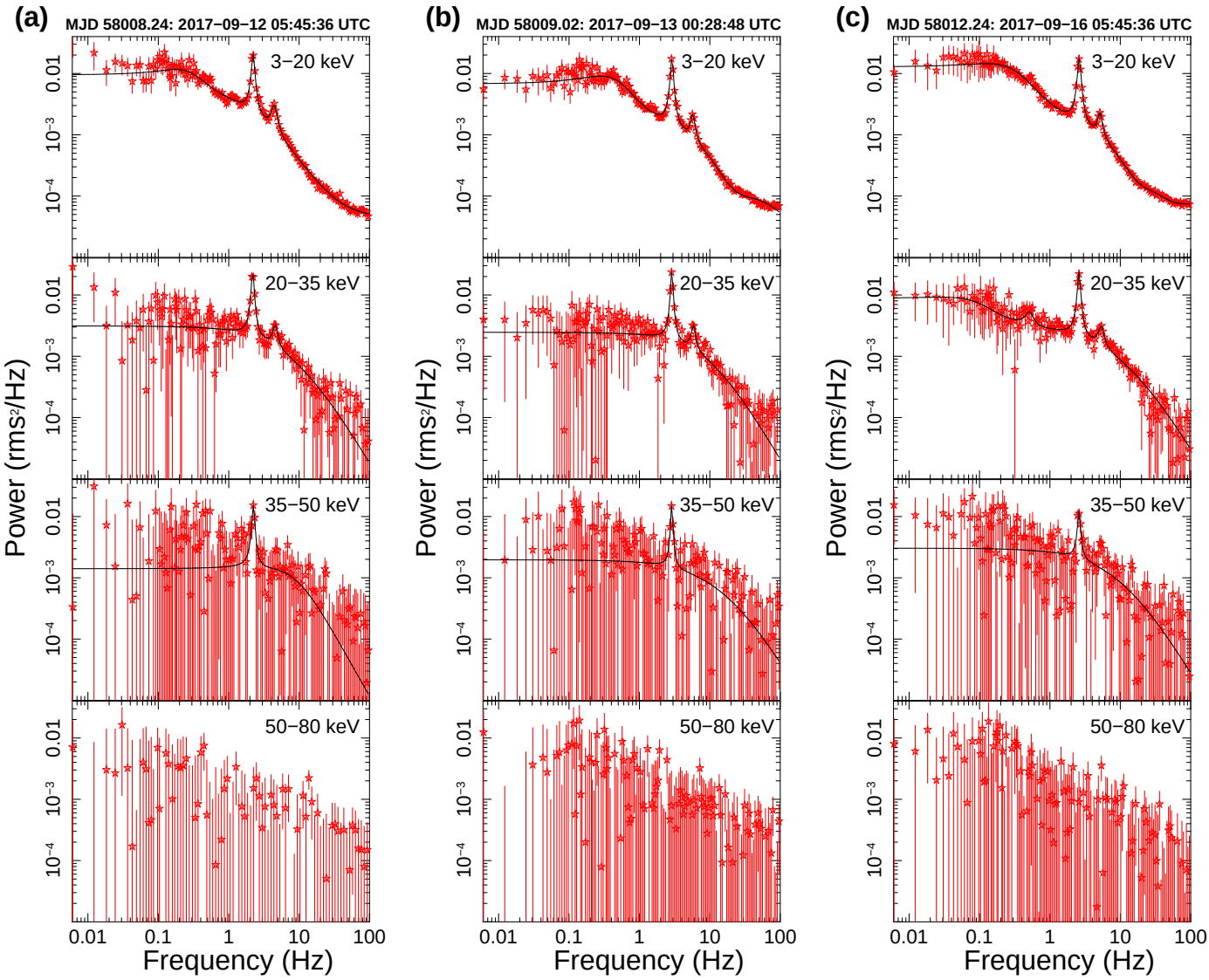


Figure 6. *AstroSat/LAXPC* energy dependent PDS: first column for MJD 58008.24 (Orbit 10585) data, middle for MJD 58009.02 (Orbit 10597) and last column for MJD 58012.24 (Orbit 10644), each for energy bands $3-20$ keV, $20-35$ keV, $35-50$ keV and $50-80$ keV respectively. There are no signatures of QPOs in the highest band of $50-80$ keV for any of the observed *AstroSat* ToO orbits. BLN and LFN are present upto 20 keV. The second harmonic of the QPO is significant only upto 35 keV. We have not modelled the PDS in $50-80$ keV as it is dominated by noise.

following energy ranges: $3-20$ keV, $20-35$ keV, $35-50$ keV and $50-80$ keV, for MJD 58008.24 (Orbit 10585), 58009.02 (Orbit 10597) and 58012.24 (Orbit 10644). Table 2 lists the energy dependent QPO parameter variations for MJDs 58008.24, 58009.02 and 58012.24. It is evident that the fundamental QPO appears in the range $3-50$ keV, while the second harmonic was significant only in the $3-35$ keV band. No QPOs were seen in $50-80$ keV band. A low frequency noise (LFN) and a band limited noise (BLN) also contributed to the power in energy range $3-20$ keV.

The evolution of QPO centroid frequency, total rms and QPO rms are presented in Figure 7. Here, *XRT* results are shown in red while *LAXPC* results are shown in blue. In order to compare results, QPO parameters were calculated in $3-10$ keV for both *XRT* and *LAXPC*. Note that, the *XRT* PDS in the $0.5-3$ keV band had no QPO like features and these photons piled-up to bring down the QPO rms values in $3-10$ keV band. Therefore, we applied pile-up correction as mentioned in §2.2 in order to estimate the correct rms in $3-10$ keV *XRT* data. It was observed that the QPO frequency did not evolve except for the first four *Swift* observations. The first QPO of 0.44 Hz was detected with *XRT* data on MJD 58004.29 when the source was in the LHS. Beyond that, the fundamental frequency was almost constant during the HIMS as indicated by both *XRT* and *LAXPC* observations. The total rms for the *LAXPC* observations was around $\sim 16.2 \pm 1.1\%$ and the corresponding QPO rms remained almost constant at $7.1 \pm 0.52\%$. The total rms in *XRT* PDS during the HIMS was around $15 \pm 2.4\%$, and the QPO rms was found to have an average value of $6.9 \pm 1.3\%$. The larger uncertainties on width and normalisation of the `Lorentzians` resulted in larger errors on rms

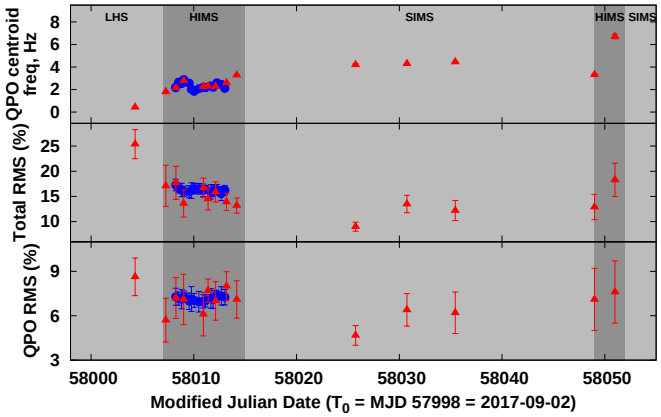


Figure 7. Evolution of QPO frequencies and corresponding RMS obtained using *LAXPC* (blue) and *XRT* (red) 3−10 keV data, are presented in the top and bottom panels respectively. The detections with both instruments overlap in the HIMS region. *LAXPC* results are dead-time corrected and *XRT* results are pile-up corrected. The variation of total rms with time is shown in the middle panel. The states of the source are also indicated as grey strips in the figure.

values. This is due to the lower photon statistics of *XRT* as compared to the high *LAXPC* count rate in $3-10$ keV band. Only three QPOs (~ 4.3 Hz) were detected between MJD 58014 and MJD 58040 with *XRT* data. During this period the source was in SIMS (Tao et al. 2018) with very high fluxes (see Figure 2). The total integrated rms in $3-10$ keV was larger during LHS and HIMS of the outburst than during the SIMS. As the source underwent a transition back to HIMS during MJD 58049 to 58051, the rms observed then was around 18%. We also detected the maximum QPO frequency (~ 6.72 Hz) from the source on MJD 58050.98. QPOs were not observed beyond this date upto MJD 58200. The presence of C-type QPOs and their frequencies indicated that the source was likely to be in HIMS during *AstroSat* observations. In §5, we have presented the results of spectral analysis and modelling with the *AstroSat* data. Further, we intended to estimate the accretion parameters of the source and constrain the mass of the black hole. It was with this motivation that we decided to use the two-component flow model (see §5.3).

5 SPECTRAL ANALYSIS AND RESULTS

5.1 Spectral Analysis

Initially, we modelled the *SXT* spectrum of MJD 58008.24 (Orbit 10585) with `Tbabs` (Wilms et al. 2000), `diskbb` and `powerlaw`. This gave an inner disc temperature of 0.23 keV and a `powerlaw` photon index of 2.31 with a χ^2/dof of $782.4/612 = 1.27$. Energy spectrum from *SXT* in the range $0.7-7$ keV was then modelled with thermally comptonized continuum - `nthComp` (Zdziarski et al. (1996), Życki et al. (1999)). We used gain correction with a fixed slope of 1 using the `gain fit` command to flatten the residuals at 1.8 and 2.2 keV. Even after that, residuals were slightly on the higher side at around 1.7 keV and below 0.8 keV. The modelling with `nthComp` gave a χ^2/dof of $866/613 = 1.41$.

Then we modelled the corresponding *LAXPC10* spectrum in the range $3-80$ keV initially with `diskbb + powerlaw` and then with `nthComp`. The fit with `Tbabs` × `(diskbb + powerlaw)` gave poor results at a $\chi^2_{red} \sim 6$ and it was found that the `diskbb` component was insensitive to the fit. The fit with `Tbabs` × `(nthComp)` was better and gave χ^2_{red} of $504/274 = 1.84$. Further, the inclusion of a `gaussian` to account for the iron line at around 6.6 keV and an instrumental Xenon `edge` around 33 keV improved the fit resulting in a χ^2_{red} of $272.8/270 = 1.01$. The strong iron line indicated the possible presence of a continuum reflection component in the spectra. In order to check this, we introduced a reflection component (`ireflect`) and found that the relative reflection coefficient was too low ($0.03 - 0.08$). Moreover, the $\chi^2/dof = 272.61/269 = 1.01$, did not improve after including reflection component. Therefore, we inferred that a reflection continuum was not required to model the energy spectra of the source using data from *AstroSat* observations. The fit results implied that when we combine *SXT* and *LAXPC* data, it was better to model with `nthComp` than using the phenomenological model containing `diskbb` and `powerlaw`.

A 2% systematic error in each bin was incorporated in the spectral response as specified in the *SXT* user manual[10] and by Leahy & Chen (2019). The systematic error for spectral data from *LAXPC* detectors was also reported to be within 2% (Antia et al. 2017). Therefore, the combined spectral fit with both *SXT* and *LAXPC* were considered to have a 2% systematic error in order to achieve a good estimate of the spectral fit parameters. Once good independent fits were obtained, we attempted for combined fitting of energy spectra with *SXT* and *LAXPC* data using `nthComp`. The `gaussian` line width was frozen to 0.6 keV for the broadband modelling. This gave a reasonable χ^2_{red} of $1181/895 = 1.31$ with a photon index of $2.254^{+0.004}_{-0.005}$, electron temperature of $37.8^{+2.74}_{-2.37}$ keV and seed photon temperature of $0.21^{+0.02}_{-0.04}$ keV on MJD 58008.24. Unless mentioned explicitly, all the errors are computed using $\Delta\chi^2 = 1.0$ (68% confidence level) for all the observations (see Table 3). Further, we carried out spectral analysis for all the observations under consideration with `nthComp` and the results are presented in §5.2.

The hydrogen column density used for this source so far by other investigators for spectral fitting are $(4.44 \pm 1.1) \times 10^{22}$ atoms cm^{-2} (Russell et al. 2018b; Parikh et al. 2018) and 4.05×10^{22} atoms cm^{-2} (Miller et al. 2018). Russell et al. (2018b) arrived at this value for N_H (with 25% error) using three observations from the declining phase of the outburst, when the source was undergoing soft to hard state transition. Tao et al. (2018); Shang et al. (2018) have left N_H parameter free. It should be noted that the HEASARC N_H calculator[11] gives hydrogen column density of only 1.46×10^{22} atoms cm^{-2}. The N_H value can change with states of the source due to variation in radio activity (jets/outflows). As *AstroSat* observations of the source were made when the radio flux varied, we attempted to determine N_H density independently from the *AstroSat* spectra.

[10] http://www.tifr.res.in/∼astrosat_sxt/dataanalysis.html
[11] https://heasarc.gsfc.nasa.gov/cgi-bin/Tools/w3nh/w3nh.pl

The combined fits with *SXT* and *LAXPC* using free N_H parameter resulted in N_H values within a narrow range of 2.52×10^{22} to 2.67×10^{22} atoms cm^{-2}. As our spectral modelling indicated minimal scatter of the N_H value, the `Tbabs` component was left free throughout our analysis.

5.2 Spectral Properties

As detailed in §5.1, the appropriate model to fit the energy spectra (in the energy range $0.7 - 80$ keV) is `Tbabs` × `constant(gaussian` + `edge` × `nthComp)`. In Figure 8, we have shown the broadband spectrum from MJD 58011.13 fitted with the above model based on `nthComp`. The photon index for this fit is 2.238 ± 0.005 with a $\chi^2_{red} = 1.19$ (1071/895) indicating that the source was in HIMS. The results of spectral modelling and the χ^2_{red} values for all observations are included in Table 3. The entries indicated with a † symbol correspond to broadband observations combining *SXT* and *LAXPC* data. All other entries in this table correspond to *LAXPC* observations alone. The model based on `nthComp` satisfactorily fits all these observations. We find that the photon index (Γ) values vary from 2.18 to 2.37 only and did not show much evolution within the six days of *AstroSat* observation. The value of electron temperature, kT_e is in the range between $21.2 - 63$ keV indicating a minimum high energy cut-off of $\sim$ 60 keV (3 kT_e). For a few observations, we were unable to constrain kT_e from the fit and in those cases we fixed it to a high value of 100 keV (see Table 3). The seed photon temperature parameter kT_{bb}, which specifies the low energy roll over varied between 0.19 to 0.29 keV. The norm remained in the range 21.6 to 53.9. A Xenon `edge` in the range $32 - 34$ keV was required in all cases. The `gaussian` line energy around 6.6 keV had width fixed to 0.6 keV. The total flux in the $0.3 - 80$ keV during the *AstroSat* observations was high and it varied from 7.14×10^{-8} to 1.10×10^{-7} erg cm^{-2} s^{-1}. Assuming the source to be at 8 kpc distance as considered by Tao et al. (2018), we computed the luminosity to be in the range between 5.46×10^{38} to 8.38×10^{38} erg s^{-1}. For a black hole of mass 6 $M_\odot$, the luminosity when expressed in terms of Eddington Luminosity is 0.70 to 1.07 L_{Edd}. Using the Γ and kT_e parameters, we also computed the optical depth (τ) of the system based on the formula given by Zdziarski et al. (1996). τ was found to be in the range $0.72 - 2.5$.

As mentioned in §4.3, the presence of strong QPOs in the power spectrum helps us to conclude that the corona is oscillating in nature. The lack of evolution in the QPO frequency and the tight range of spectral photon indices both point to the fact that the corona is of almost constant size during the *AstroSat* observations. In the next section, we present the details of spectral modelling with two-component accretion flow and determine the shock location which indicates the size of the PSC. We also attempt to constrain the mass of the source using the same model.

5.3 Spectral modelling: two-component accretion flow

Further, we have used the two-component accretion flow (Chakrabarti & Titarchuk 1995; Chakrabarti & Mandal 2006) to model the broadband energy spectra ($0.7 - 80$ keV) using spectral data from *SXT* and *LAXPC*. In this model, a Keplerian disc is situated at the equatorial plane of the binary system and a sub-Keplerian halo component resides on top and bottom of the Keplerain disc. The inner boundary condition of the accretion flow around a black hole demands a supersonic flow and the rotating supersonic flow faces a virtual centrifugal barrier close to the horizon. This triggers a shock discontinuity in the accretion flow (Fukue 1987; Chakrabarti 1989) and the flow becomes sub-sonic after passing through a shock. Here, the kinetic energy gets converted into thermal energy and this 'hot' region beyond the shock is referred to as the post-shock corona (PSC). The Keplerian disc produces multi-colour blackbody photons and a significant fraction of these photons intercept the 'hot' PSC. The high energy photons are formed due to the inverse Comptonisation of soft photons from the Keplerian disc in the PSC. This model has five parameters (see Iyer et al. 2015) namely the mass of the black hole (M), the shock location (x_s), the sub-Keplerian halo rate ($\dot{m}_h$), Keplerian disc accretion rate ($\dot{m}_d$) and free normalisation constant. Here, mass of the black hole is expressed in solar mass unit ($M_\odot$), radial distance is expressed in Schwarzschild radii ($r_g = 2GM/c^2$), where G is gravitational constant and c is the speed of light in vacuum. The accretion rate is expressed in unit of Eddington rate ($\dot{m}_{Edd}$).

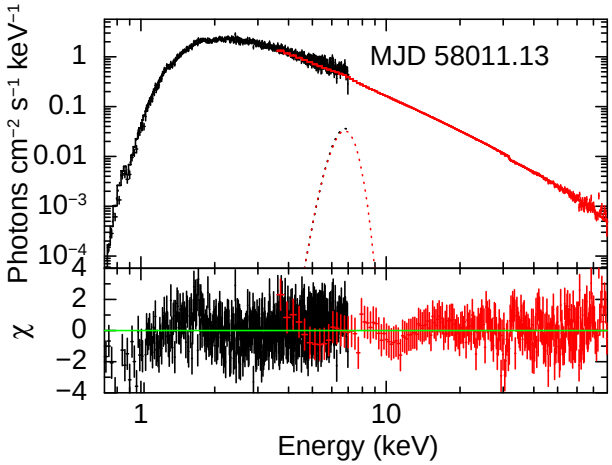


Figure 8. Broadband spectrum in the energy range $0.7 - 80$ keV using data from both *SXT* ($0.7 - 7$ keV) and *LAXPC* ($3 - 80$ keV) onboard *AstroSat* corresponding to MJD 58011.13 (Orbit 10628). *SXT* data are shown in black and *LAXPC* data are shown in red. The spectrum is fitted with continuum thermal Comptonisation model (`nthComp`). The source was in HIMS during this observation with a photon index of 2.238 ± 0.005.

This model is implemented in `XSPEC` as a table model (Iyer et al. 2015). In Figure 9, we have presented a fit of combined spectrum of *SXT+LAXPC* data corresponding to MJD 58011.13 (Orbit number 10628) using two-component model along with an additional `highecut` component of `XSPEC`. The `gaussian` and `edge` components used in our earlier model was required here as well. The disc and halo accretion rates are respectively $0.977^{+0.109}_{-0.157}$ and $0.203^{+0.019}_{-0.022}$ $\dot{m}_{Edd}$. The corresponding shock location is $16.3^{+0.80}_{-0.99}$ r_g. The mass of the black hole obtained by modelling this particular observation with the two-component flow model is $6.31^{+0.68}_{-0.86}$

Table 3. Spectral parameters resulting from a fit with the model `Tbabs` × `constant` × (`gaussian` + `edge` × `nthComp`). † denotes broadband modelling with *SXT* and *LAXPC*, whereas other observations are modelled using data from *LAXPC* instrument alone. Unabsorbed flux values in 0.3 − 80 keV are also included in the Table.

MJD	Orbit	Γ	kT$_e$ (keV)	kT$_{bb}$ (keV)	norm	flux (0.3 − 80 keV) (erg cm^{-2} s^{-1})	τ	χ^2_{red} (χ^2/dof)
58008.24 †	10585	$2.254^{+0.004}_{-0.005}$	$37.8^{+2.7}_{-2.3}$	$0.21^{+0.02}_{-0.04}$	$34.3^{+2.6}_{-1.5}$	7.14×10^{-8}	1.640 ± 0.011	1.31 (1181/895)
58008.53 †	10589	$2.346^{+0.004}_{-0.005}$	100.0 (fixed)	$0.19^{+0.03}_{-0.04}$	$43.5^{+0.3}_{-0.3}$	8.68×10^{-8}	0.720 ± 0.004	1.25 (1127/896)
58008.82 †	10594	$2.316^{+0.003}_{-0.003}$	100.0 (fixed)	$0.19^{+0.05}_{-0.05}$	$35.3^{+0.3}_{-0.4}$	8.63×10^{-8}	0.739 ± 0.004	1.27 (1140/896)
58009.02	10597	$2.374^{+0.006}_{-0.005}$	$63.0^{+10.2}_{-6.9}$	$0.20^{+0.008}_{-0.009}$	$34.7^{+2.2}_{-8.3}$	7.17×10^{-8}	1.010 ± 0.008	1.14 (311/271)
58009.55 †	10604	$2.327^{+0.003}_{-0.003}$	100.0 (fixed)	$0.22^{+0.01}_{-0.03}$	$43.4^{+5.2}_{-5.5}$	9.21×10^{-8}	0.732 ± 0.004	1.41 (1268/896)
58009.77	10608	$2.243^{+0.005}_{-0.004}$	$39.1^{+2.9}_{-2.3}$	$0.24^{+0.006}_{-0.008}$	$25.2^{+4.1}_{-8.3}$	7.29×10^{-8}	1.612 ± 0.009	1.15 (312/271)
58010.03	10612	$2.189^{+0.005}_{-0.004}$	$24.2^{+0.8}_{-0.6}$	$0.29^{+0.03}_{-0.12}$	$21.6^{+0.5}_{-7.1}$	7.41×10^{-8}	2.380 ± 0.010	1.09 (296/271)
58010.49 †	10618	$2.233^{+0.005}_{-0.002}$	$32.6^{+1.3}_{-1.2}$	$0.21^{+0.01}_{-0.07}$	$38.2^{+0.3}_{-0.3}$	9.39×10^{-8}	1.856 ± 0.012	1.26 (1131/895)
58010.92 †	10625	$2.261^{+0.006}_{-0.005}$	$33.0^{+1.9}_{-1.5}$	$0.24^{+0.04}_{-0.04}$	$38.1^{+0.5}_{-0.5}$	9.32×10^{-8}	1.798 ± 0.014	1.09 (945/866)
58011.13 †	10628	$2.238^{+0.005}_{-0.005}$	$21.2^{+0.6}_{-0.5}$	$0.19^{+0.04}_{-0.04}$	$31.6^{+2.2}_{-1.8}$	9.43×10^{-8}	2.514 ± 0.012	1.19 (1071/895)
58011.66 †	10636	$2.287^{+0.009}_{-0.004}$	$41.2^{+2.9}_{-2.4}$	$0.20^{+0.02}_{-0.05}$	$46.1^{+0.2}_{-0.3}$	1.03×10^{-7}	1.504 ± 0.010	1.34 (1202/895)
58011.87	10639	$2.281^{+0.005}_{-0.004}$	$36.5^{+2.5}_{-2.1}$	$0.22^{+0.006}_{-0.008}$	$31.6^{+2.4}_{-6.5}$	7.96×10^{-8}	1.645 ± 0.009	1.29 (351/271)
58012.24 †	10644	$2.327^{+0.005}_{-0.005}$	$26.1^{+1.0}_{-0.8}$	$0.22^{+0.004}_{-0.003}$	$52.0^{+0.4}_{-0.4}$	1.03×10^{-7}	2.038 ± 0.010	1.21 (1091/895)
58012.67 †	10651	$2.316^{+0.003}_{-0.005}$	$54.4^{+4.8}_{-4.4}$	$0.19^{+0.03}_{-0.01}$	$53.9^{+0.4}_{-2.5}$	1.10×10^{-7}	1.188 ± 0.009	1.51 (1353/895)
58013.02	10656	$2.249^{+0.005}_{-0.004}$	$23.6^{+0.81}_{-0.58}$	$0.29^{+0.005}_{-0.005}$	$28.4^{+0.71}_{-8.6}$	8.48×10^{-8}	2.317 ± 0.012	1.05 (285/271)

Table 4. Fit parameters from the model `TBabs` × `constant(gaussian` + `edge` × `highecut` × `two-component-flow)` applied on *AstroSat* data.

MJD	58011.13	58012.24
Orbit	10628	10644
Mass ($M_\odot$)	$6.31^{+0.68}_{-0.86}$	$6.47^{+1.36}_{-1.33}$
Shock location (r_g)	$16.3^{+0.80}_{-0.99}$	$15.9^{+2.1}_{-0.8}$
Halo rate ($\dot{m}_{Edd}$)	$0.203^{+0.019}_{-0.022}$	$0.15^{+0.02}_{-0.02}$
Disc rate ($\dot{m}_{Edd}$)	$0.977^{+0.109}_{-0.157}$	$0.78^{+0.15}_{-0.20}$
Cutoff Energy (keV)	$20.0^{+1.2}_{-1.4}$	$18.9^{+1.1}_{-0.89}$
Fold Energy (keV)	$78.6^{+8.0}_{-7.8}$	$85.2^{+5.8}_{-4.7}$
χ^2/dof	1.15 (1031.32/891)	1.19 (1063.99/891)

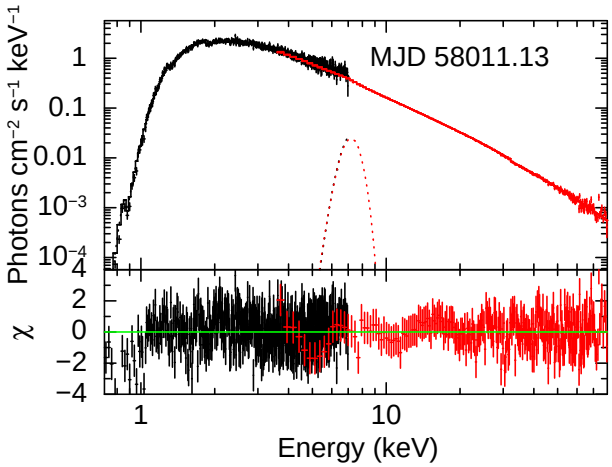


Figure 9. Broadband 0.7 − 80 keV spectrum for Orbit 10628 (MJD 58011.13) of *AstroSat*, using data from both *SXT* (0.7 − 7 keV) and *LAXPC* (3 − 80 keV). *SXT* data is indicated using black colour and *LAXPC* data is shown in red colour. The spectrum is fitted with two-component accretion flow model. See text for results.

$M_\odot$. In Table 4, we have presented the results of broadband spectral fitting using two-component accretion flow model (at 90% confidence level) for two representative cases and observed that the spectral state of the source did not change much. Model fitting for the two observations considered suggests that the possible mass of the BH source is in the range 5.14 − 7.83 $M_\odot$ and the relative accretion rate (see Table 4) indicates the source to be in intermediate state (Nandi et al. 2018). We have chosen two broadband (0.7 − 80 keV) observations (MJD 58011.13 and 58012.24) for two-component flow modelling as the QPO frequencies in these cases are not the same. We expect that the shock location which is an estimate of the size of the PSC decreases with an increase in QPO frequency. The results of physical modelling and temporal modelling indicates the same, as we have a shock location of ∼ 16.3 r_g and QPO frequency of ∼ 2.17 Hz on MJD 58011.13, while the shock location on MJD 58012.24 is only ∼ 15.9 r_g corresponding to a higher QPO frequency of ∼ 2.59 Hz (see Tables 1 and 4). Also, the relative disc to halo accretion rates in both cases are similar, indicating that the source has not undergone a state transition during the *AstroSat* observations.

This model has a free normalisation which is a function of inclination angle and distance to the source. The normalisation constant shifts the scale of the overall luminosity of the source. The mass and accretion rates are independent quantities in the model and both determine the source luminosity as well as the spectral characteristics. In fact, for a given mass, the change in accretion rates determines the spectral evolution during the outburst. Hence, only a specific range of mass can model all the observed data. We believe that the observed data may include some contributions from the base of the jet, particularly in intermediate states. This is not considered in the current model. Also, as discussed in §6, the spin parameter of the black hole is not taken into account in this model. With the inclusion of these contributions in the model, the estimated accretion parameters may differ slightly.

6 DISCUSSION AND CONCLUSIONS

The *MAXI* detection of a bright X-ray transient lead to a large follow up observation campaign with multiple observatories following the outburst. These observations point to the black hole binary nature of this source, which shows state transitions similar to a canonical black hole binary. *AstroSat* made a few observations in the intermediate state of the source. In this paper, we have studied the outbursting source MAXI J1535−571 using four different instruments namely *MAXI*, *Swift/XRT*, *AstroSat/SXT* and *AstroSat/LAXPC*. Using *MAXI*, we have studied the outburst profile (Figure 2) and the HID (Figure 3) of the entire outburst. This source showed a slightly unusual HID evolution with extremely high flux seen in the intermediate states before it dimmed considerably during its transition towards the soft state. The source has gone through LHS, HIMS, SIMS, HIMS, SIMS and soft state in the rising phase. We have not considered data beyond MJD 58200 due to weak activity of the source leading to large errorbars in counts, though Tao et al. (2018) have classified the source to be in soft state from MJD 58137 to 58230.

We made use of observations from *XRT* to study the state transitions based on the HRD and RID. From the HRD (Figure 5a) it is evident that the hardness decreases as the states evolve and rms is comparatively lower during the SIMS. The RID (Figure 5b) suggests that the rms is larger during the harder states as expected and is low during the SIMS which corresponds to the highest count rate. The *AstroSat* observations of the source shaded in Figures 5a and 5b falls in the HIMS region.

XRT and *LAXPC* data were used to carry out timing analysis of the source. We detected C-type QPOs in the range 1.85−2.88 Hz along with second harmonics during the rising phase of the outburst with *LAXPC* data. The power spectra also showed band limited noise and low frequency noise. We confirm that this period corresponds to the HIMS phase of the outburst as classified by Tao et al. (2018); Huang et al. (2018). Using *HXMT* data, Huang et al. (2018) have detected QPOs upto 100 keV, though *LAXPC* showed no evidence of QPOs beyond 50 keV. This is probably due to the fact that the *LAXPC* has only an effective area in the range 4100 cm^2 to 2200 cm^2 as energy changes from 60 keV to 80 keV (Antia et al. 2017), whereas *HXMT* has a higher effective area of 5100 cm^2 in the $20-250$ keV energy range (Li et al. 2018). QPOs are thought to be signatures of physical oscillations in the accreting flow and many reasons have been proposed for explaining the presence of such oscillations. Magneto-rotational instabilities (MRIs) in the accretion disc (Machida & Matsumoto 2008) can be a reason for QPOs. During the process of accretion, when the magnetic energy accumulated in an accretion disc at a particular stage is released, the disc becomes weakly magnetized and axisymmetric. The magnetic energy again gets amplified due to MRI and the cycle repeats. The period of these cycles results in low frequency peaks around 4 to 8 Hz. LFQPOs in black hole binaries can possibly be generated due to these magnetic cycles. Lense-Thirring effects in the accretion disc (Ingram et al. 2009) may also be a reason for QPOs. In this case, the rotation of the central black hole causes frame-dragging in the vicinity of the black hole. This in turn, causes the orbits of particles in the accretion disc to precess and the associated precession frequency is found to be close to observed QPO frequencies. In this work, we consider the two-component accretion flow framework, under which an oscillating PSC (Chakrabarti et al. 2008) can cause these QPOs.

It is evident from the energy dependent analysis of power spectra that the QPO rms exceeded ∼8% in 3−20 keV energy band. It increased up to ∼9% in the $20-35$ keV range and in the $35-50$ keV energy band the QPO rms decreased slightly to $6-7\%$. Rodriguez et al. (2002) have reported similar energy dependence of LFQPOs for GRS 1915+105. Rao Jassal et al. (2016) have studied the connection between the QPOs and the spectral components and have shown that a small in-phase variation of the spectral index with the QPO could reproduce the energy dependence of QPO rms. This is consistent with the origin of LFQPOs due to oscillation of PSC. For a given QPO frequency, the PSC will oscillate with respect to an average position. During oscillation, as PSC expands the spectral index decreases (i.e. harder spectrum) and when the PSC shrinks the spectral index increases. This behaviour is same as the change in spectral index due to the change in the shock location as shown in Mandal & Chakrabarti (2005).

Further, *SXT+LAXPC* combined broadband spectra were analysed to examine the source characteristics. Initially, the spectra were modelled with a thermally Comptonised continuum (`nthComp`) along with a Xenon `edge` and an iron line (`gaussian`). The seed photon temperature was consistently in 0.19 to 0.29 keV range. The high energy cut off was at least ∼ 60 keV as inferred from the electron temperature (kT_e). The photon index of the energy spectrum was in a narrow range of $2.18-2.37$ throughout the observations with *AstroSat*. This along with the lack of QPO frequency evolution indicates that the oscillating post shock corona was almost constant in size during this period. The phenomenological modelling implies that the spectrum was completely dominated by thermal Comptonisation. The absence of a separate disc component in the model, suggests that disc was either truncated away as indicated by the low seed photon temperature or was buried within the corona. The soft photons supplied by the disc enters into the corona which has a moderate optical depth ($0.72 < \tau < 2.5$) and produces the strong comptonised component.

Moreover, as the relative reflection coefficient was not significant in the energy spectra of HIMS observations with *AstroSat*, we expected that the iron abundance must be high to get a strong iron line feature. In order to verify the results, we modelled the $SXT + LAXPC$ broadband spectra of HIMS with `relxillCp` (García et al. 2014), which includes Comptonisation and reflection taking into consideration the iron abundance. The value of reflection coefficient obtained from `relxillCp` was 0.07 ± 0.02 and the iron abundance was in the range between $1.2-1.7$ times solar abundance. The larger than solar abundance levels of iron caused the strong iron lines in the energy spectra. The iron abundance is comparable to the value $1.4^{+0.3}_{-0.1}$ times solar abundance, as obtained by Xu et al. (2018), during LHS (MJD 58003). The equivalent width (EW) of the iron line was ∼ 0.11 keV, which falls in the range between 0.05 keV to 0.3 keV, typical for black hole binaries (Gilfanov 2010).

Besides this, we modelled the combined $SXT + LAXPC$ energy spectra using the two-component accretion flow

model. The results from Table 4 show that the Keplerian-disc accretion rate is around the Eddington accretion limit. Similar rates are seen in XTE J1859+226 (Nandi et al. 2018) during its HIMS, but not usually seen in other black hole binaries (see Iyer et al. 2015; Radhika et al. 2018). The near Eddington accretion rates (see Table 4) observed in the intermediate states seem to be the reason for the excessive brightening of the source with luminosity as high as 1.07 L_{Edd} (see Table 3 and §5.2). High accretion rates can trigger outflows to escape from the accretion stream, which can be observationally seen as radio emissions (Radhika & Nandi 2014; Radhika et al. 2016). The large absorption columns reported (as compared to the expected galactic column from HI maps) also point to the presence of some outflows. Baglio et al. (2018) report wild infra-red flickering during this period, consistent with erratic outflows.

The spectral modelling with two-component flow suggests a compact corona of almost constant size ($\sim 16\ r_g$). As a result, the C-type QPOs formed due to the oscillations of the corona are in a narrow range of frequencies as observed from *LAXPC* data. It should be noted that, the model is applicable only for a stationary black hole. The effect of black hole spin on the radiation spectrum is that the spectrum gets harder (Mandal & Mondal 2018) as the black hole spins faster. Hence, inclusion of black hole spin will change the estimated value of the size of PSC for a given data set. In future, we aim to model the spectral data including the black hole spin.

Finally, physical modelling of the energy spectra from *AstroSat* observations based on the two-component accretion flow model suggests that the source hosts a black hole of mass 5.14−7.83 $M_{\odot}$, which is similar to other Galactic black hole binaries (Corral-Santana et al. 2016; Tetarenko et al. 2016; Nandi et al. 2018). In summary, we have characterised the spectro-temporal properties of the source MAXI J1535−571 using *AstroSat* data during its 2017 outburst with the help of *MAXI* and *Swift* results.

ACKNOWLEDGEMENT

Authors are thankful to the reviewer for his/her valuable suggestions and comments that helped to improve the quality of the manuscript. We acknowledge the clarifications that we got from Dr. Matteo Bachetti regarding dead-time effects. We are thankful to the *Swift* help desk for the information on pile-up and dead-time effects in *XRT*. This research has made use of data obtained through the High Energy Astrophysics Science Archive Research Center (HEASARC) online service, provided by the NASA/Goddard Space Flight Center. This publication uses the data from the *AstroSat* mission of the Indian Space Research Organisation (ISRO), archived at the Indian Space Science Data Centre (ISSDC). This work has used the data from the Soft X-ray Telescope (*SXT*) developed at TIFR, Mumbai, and the *SXT* POC at TIFR is thanked for verifying & releasing the data and providing the necessary software tools. This work has also used the data from the *LAXPC* Instruments developed at TIFR, Mumbai, and the *LAXPC* POC at TIFR is thanked for verifying & releasing the data. We thank the *AstroSat* Science Support Cell hosted by IUCAA and TIFR for providing the `LaxpcSoft` software which we used for *LAXPC* data analysis. AN thanks GD, SAG; DD, PDMSA and Director, URSC for encouragement and continuous support to carry out this research.

REFERENCES

Agrawal V. K., Nandi A., Girish V., Ramadevi M. C., 2018, MNRAS, 477, 5437
Antia H. M., et al., 2017, ApJS, 231, 10
Bachetti M., et al., 2015, ApJ, 800, 109
Baglio M. C., et al., 2018, ApJ, 867, 114
Belloni T. M., Motta S. E., 2016, in Bambi C., ed., Astrophysics and Space Science Library Vol. 440, Astrophysics of Black Holes: From Fundamental Aspects to Latest Developments. p. 61 (arXiv:1603.07872), doi:10.1007/978-3-662-52859-4_2
Belloni T., Homan J., Casella P., Van Der Klis M., Nespoli E., Lewin W., Miller J., Méndez M., 2005, Astronomy & Astrophysics, 440, 207
Casella P., Belloni T., Stella L., 2005, ApJ, 629, 403
Chakrabarti S. K., 1989, ApJ, 347, 365
Chakrabarti S. K., Mandal S., 2006, ApJ, 642, L49
Chakrabarti S., Titarchuk L. G., 1995, ApJ, 455, 623
Chakrabarti S. K., Debnath D., Nandi A., Pal P. S., 2008, A&A, 489, L41
Corral-Santana J. M., Casares J., Muñoz-Darias T., Bauer F. E., Martínez-Pais I. G., Russell D. M., 2016, A&A, 587, A61
Das S., Chattopadhyay I., Nandi A., Molteni D., 2014, MNRAS, 442, 251
Fukue J., 1987, PASJ, 39, 309
García J., et al., 2014, ApJ, 782, 76
Gilfanov M., 2010, in Belloni T., ed., Lecture Notes in Physics, Berlin Springer Verlag Vol. 794, Lecture Notes in Physics, Berlin Springer Verlag. p. 17 (arXiv:0909.2567), doi:10.1007/978-3-540-76937-8_2
Homan J., Belloni T., 2005, Ap&SS, 300, 107
Homan J., Wijnands R., van der Klis M., Belloni T., van Paradijs J., Klein-Wolt M., Fender R., Méndez M., 2001, ApJS, 132, 377
Huang Y., et al., 2018, preprint, (arXiv:1808.05318)
Ingram A., Done C., Fragile P. C., 2009, MNRAS, 397, L101
Iyer N., Nandi A., Mandal S., 2015, Astrophysical Journal, 807, 108
Kennea J. A., 2017, The Astronomer's Telegram, 10731
Kennea J. A., Evans P. A., Beardmore A. P., Krimm H. A., Romano P., Yamaoka K., Serino M., Negoro H., 2017, The Astronomer's Telegram, 10700
Leahy D. A., Chen Y., 2019, ApJ, 871, 152
Li T., et al., 2018, Science China Physics, Mechanics, and Astronomy, 61, 31011
Machida M., Matsumoto R., 2008, PASJ, 60, 613
Mandal S., Chakrabarti S. K., 2005, A&A, 434, 839
Mandal S., Mondal S., 2018, Journal of Astrophysics and Astronomy, 39, 19
Mereminskiy I. A., Grebenev S. A., 2017, The Astronomer's Telegram, 10734
Mereminskiy I. A., Grebenev S. A., Prosvetov A. V., Semena A. N., 2018, Astronomy Letters, 44, 378
Miller J. M., et al., 2018, ApJ, 860, L28
Misra R., et al., 2017, ApJ, 835, 195
Mitsuda K., et al., 1984, PASJ, 36, 741
Motta S., Homan J., Muñoz Darias T., Casella P., Belloni T. M., Hiemstra B., Méndez M., 2012, MNRAS, 427, 595
Muñoz-Darias T., Motta S., Stiele H., Belloni T. M., 2011, MNRAS, 415, 292
Nakahira S., et al., 2017, The Astronomer's Telegram, 10729
Nakahira S., et al., 2018, preprint, (arXiv:1804.00800)

Nandi A., Debnath D., Mandal S., Chakrabarti S. K., 2012, A&A, 542, A56
Nandi A., et al., 2018, Ap&SS, 363, 90
Negoro H., et al., 2017a, The Astronomer's Telegram, 10699
Negoro H., et al., 2017b, The Astronomer's Telegram, 10708
Negoro H., et al., 2018a, The Astronomer's Telegram, 11568
Negoro H., et al., 2018b, The Astronomer's Telegram, 11682
Palmer D. M., Krimm H. A., Swift/BAT Team 2017, The Astronomer's Telegram, 10733
Parikh A. S., Russell T. D., Wijnands R., Bahramain A., Miller-Jones J. C. A., Tetarenko A. J., Sivakoff G. R., 2018, The Astronomer's Telegram, 11652
Radhika D., Nandi A., 2014, Advances in Space Research, 54, 1678
Radhika D., Nandi A., Agrawal V. K., Seetha S., 2016, MNRAS, 460, 4403
Radhika D., Sreehari H., Nandi A., Iyer N., Mandal S., 2018, Ap&SS, 363, 189
Rao Jassal A., Vadawale S. V., Mithun N. P. S., Misra R., 2016, ApJ, 817, 28
Remillard R. A., McClintock J. E., 2006, ARA&A, 44, 49
Rodriguez J., Durouchoux P., Mirabel I. F., Ueda Y., Tagger M., Yamaoka K., 2002, A&A, 386, 271
Russell T. D., Miller-Jones J. C. A., Sivakoff G. R., Tetarenko A. J., Jacpot Xrb Collaboration 2017a, The Astronomer's Telegram, 10711
Russell T. D., Altamirano D., Tetarenko A. J., Sivakoff G. R., Neilsen J., Miller-Jones J. C. A., van den Eijnden J., Jacpot Xrb Collaboration 2017b, The Astronomer's Telegram, 10899
Russell T., Russell D., Altamirano D., Miller-Jones J., Sivakoff G., Tetarenko A., 2018a, in 42nd COSPAR Scientific Assembly. pp E1.4–54–18
Russell T. D., Altamirano S. R. D., Miller-Jones J. C. A., Plotkin R., Tetarenko A. J., Sivakoff G. R., JACPOT XRB Collaboration 2018b, The Astronomer's Telegram, 11611
Seward F. D., Charles P. A., 2010, Exploring the X-ray Universe. Cambridge University Press, 2010. ISBN: 9780521884839
Shakura N. I., Sunyaev R. A., 1973, A&A, 24, 337
Shang J.-R., Debnath D., Chatterjee D., Jana A., Chakrabarti S. K., Chang H.-K., Yap Y.-X., Chiu J.-L., 2018, preprint, (arXiv:1806.07147)
Shidatsu M., et al., 2017, The Astronomer's Telegram, 11020
Singh K. P., et al., 2016, in Space Telescopes and Instrumentation 2016: Ultraviolet to Gamma Ray. p. 99051E, doi:10.1117/12.2235309
Singh K. P., et al., 2017, Journal of Astrophysics and Astronomy, 38, 29
Stevens A. L., et al., 2018, ApJ, 865, L15
Stiele H., Kong A. K. H., 2018, ApJ, 868, 71
Sunyaev R. A., Titarchuk L. G., 1980, A&A, 86, 121
Tanaka Y., Lewin W. H. G., 1995, X-ray Binaries, pp 126–174
Tao L., et al., 2018, MNRAS, 480, 4443
Tetarenko B. E., Sivakoff G. R., Heinke C. O., Gladstone J. C., 2016, ApJS, 222, 15
Tetarenko A. J., Russell T. D., Miller-Jones J. C. A., Sivakoff G. R., Jacpot Xrb Collaboration 2017, The Astronomer's Telegram, 10745
Titarchuk L., 1994, ApJ, 434, 570
Vadawale S. V., et al., 2016, in Space Telescopes and Instrumentation 2016: Ultraviolet to Gamma Ray. p. 99051G (arXiv:1609.00538), doi:10.1117/12.2235373
Verdhan Chauhan J., et al., 2017, ApJ, 841, 41
Wilms J., Allen A., McCray R., 2000, ApJ, 542, 914
Xu Y., et al., 2018, ApJ, 852, L34
Yadav J. S., et al., 2016a, ApJ, 833, 27
Yadav J. S., et al., 2016b, in Space Telescopes and Instrumentation 2016: Ultraviolet to Gamma Ray. p. 99051D, doi:10.1117/12.2231857
Zdziarski A. A., Johnson W. N., Magdziarz P., 1996, MNRAS, 283, 193
Życki P. T., Done C., Smith D. A., 1999, MNRAS, 309, 561
van der Klis M., 1989, in Ögelman H., van den Heuvel E. P. J., eds, NATO Advanced Science Institutes (ASI) Series C Vol. 262, NATO Advanced Science Institutes (ASI) Series C. p. 27

Table A1. Observations with *AstroSat*: ObsID T01_191T01_9000001536 between 12th Sep till 17th Sep, 2017. Fifteen orbits chosen are bold-faced.

Orb-#	Exp Time (s)	Start Time (UTC)	End Time (UTC)
10584	496.953770123	2017-09-12 05:32:33	2017-09-12 06:04:44
10585	4941.77365309	2017-09-12 05:55:48	2017-09-12 07:50:36
10586	5357.744978	2017-09-12 07:35:51	2017-09-12 09:36:54
10588	7382.02297796	2017-09-12 09:25:32	2017-09-12 12:50:29
10589	4583.00317103	2017-09-12 12:45:50	2017-09-12 14:49:28
10590	4031.87576006	2017-09-12 14:36:24	2017-09-12 16:33:09
10592	3851.26237635	2017-09-12 16:21:05	2017-09-12 18:16:50
10593	3531.06603971	2017-09-12 18:08:39	2017-09-12 20:00:38
10594	3292.33470635	2017-09-12 19:50:12	2017-09-12 21:43:51
10595	2970.22884139	2017-09-12 21:33:21	2017-09-12 23:28:27
10596	3249.72885065	2017-09-12 22:59:54	2017-09-13 01:12:44
10597	3264.45310393	2017-09-13 00:39:54	2017-09-13 03:02:45
10598	4230.74553183	2017-09-13 02:39:27	2017-09-13 04:45:33
10599	4552.78409085	2017-09-13 04:28:08	2017-09-13 06:28:26
10600	5069.68189324	2017-09-13 06:13:33	2017-09-13 08:13:57
10603	12317.7855291	2017-09-13 08:06:35	2017-09-13 13:29:21
10604	3694.92741311	2017-09-13 13:21:28	2017-09-13 15:11:56
10606	3628.15777545	2017-09-13 15:04:25	2017-09-13 16:55:33
10607	3874.79451605	2017-09-13 16:42:45	2017-09-13 18:39:45
10608	3442.76126461	2017-09-13 18:31:27	2017-09-13 20:23:45
10609	3070.35393815	2017-09-13 20:14:13	2017-09-13 22:05:06
10610	3307.57441911	2017-09-13 21:48:02	2017-09-13 23:50:57
10611	3153.40418664	2017-09-13 23:31:51	2017-09-14 01:35:17
10612	4134.9651357	2017-09-14 00:46:03	2017-09-14 03:25:09
10613	4389.06476232	2017-09-14 03:03:45	2017-09-14 05:08:50
10614	4761.01065524	2017-09-14 04:47:38	2017-09-14 06:52:10
10615	5219.04197027	2017-09-14 06:39:20	2017-09-14 08:38:08
10617	8634.5027135	2017-09-14 08:25:20	2017-09-14 12:07:52
10618	4120.10051683	2017-09-14 11:56:09	2017-09-14 13:51:28
10619	3991.58977488	2017-09-14 13:39:03	2017-09-14 15:34:31
10621	3821.43898252	2017-09-14 15:23:18	2017-09-14 17:18:31
10622	3667.28994137	2017-09-14 17:09:19	2017-09-14 19:02:57
10623	3609.30743047	2017-09-14 18:49:47	2017-09-14 20:47:03
10624	3379.89339639	2017-09-14 20:31:08	2017-09-14 22:30:13
10625	3406.84135797	2017-09-14 22:09:55	2017-09-15 00:14:39
10626	3357.2935165	2017-09-14 23:43:14	2017-09-15 01:59:46
10627	4507.45603695	2017-09-15 01:13:12	2017-09-15 03:48:27
10628	4542.56313907	2017-09-15 03:10:26	2017-09-15 05:31:16
10629	4904.77152288	2017-09-15 05:22:25	2017-09-15 07:15:57
10632	12804.8367192	2017-09-15 07:02:51	2017-09-15 12:31:09
10633	4078.40076538	2017-09-15 12:18:56	2017-09-15 14:14:48
10635	3657.04443797	2017-09-15 14:06:59	2017-09-15 15:57:55
10636	3488.04376683	2017-09-15 15:50:31	2017-09-15 17:41:02
10637	3765.87370964	2017-09-15 17:28:37	2017-09-15 19:25:07
10638	3336.03761904	2017-09-15 19:15:16	2017-09-15 21:08:22
10639	3148.43251339	2017-09-15 20:56:25	2017-09-15 22:53:34
10640	3081.41305334	2017-09-15 22:37:55	2017-09-16 00:38:52
10641	3561.31836302	2017-09-16 00:03:14	2017-09-16 02:22:36
10642	4247.31112233	2017-09-16 01:51:34	2017-09-16 04:11:31
10643	4544.92289703	2017-09-16 03:54:46	2017-09-16 05:54:00
10644	4903.1540284	2017-09-16 05:46:24	2017-09-16 07:40:10
10646	8637.82817281	2017-09-16 07:33:24	2017-09-16 11:09:57
10647	3889.49490765	2017-09-16 11:03:05	2017-09-16 12:54:18
10648	3992.12343246	2017-09-16 12:41:34	2017-09-16 14:37:30
10650	3518.57945908	2017-09-16 14:29:53	2017-09-16 16:20:18
10651	3424.59817114	2017-09-16 16:13:03	2017-09-16 18:04:24
10652	3822.22094573	2017-09-16 17:50:32	2017-09-16 19:48:56
10653	3282.38882317	2017-09-16 19:36:53	2017-09-16 21:30:31
10654	3198.43616311	2017-09-16 21:16:46	2017-09-16 23:15:04
10655	3446.71049657	2017-09-16 22:41:34	2017-09-17 01:00:46
10656	3721.80164763	2017-09-17 00:29:54	2017-09-17 02:46:05
10657	2967.15269032	2017-09-17 02:21:23	2017-09-17 03:42:35

APPENDIX A: OBSERVATIONS WITH *ASTROSAT*

APPENDIX B: OBSERVATIONS WITH *SWIFT*

Table B1. *Swift* Public archive. Selected datasets used in our analysis have bold-faced ObsIds.

ObsId	Start Time (UTC)	XRT Exp (s)
00770431000	2017-09-02 19:44:52	1615.85
00770431001	2017-09-02 22:11:56	3387.90
00770502000	2017-09-03 08:44:02	75.03
00770656000	2017-09-04 13:29:33	15.59
00770656001	2017-09-04 17:10:06	988.79
00770656002	2017-09-05 05:17:20	4504.50
00010264002	2017-09-06 00:38:57	449.22
00010264003	2017-09-08 06:38:57	4948.52
00771371000	2017-09-08 07:58:07	69.12
00010264004	2017-09-11 06:32:57	1089.60
00010264005	2017-09-12 06:16:57	899.60
00010264007	2017-09-13 00:08:57	889.45
00010264006	2017-09-14 22:17:57	1074.60
00010264008	2017-09-15 09:15:57	984.63
00010264009	2017-09-16 02:44:57	1059.78
00088245001	2017-09-17 04:14:57	2223.08
00010264010	2017-09-18 04:10:56	1104.60
00010264011	2017-09-19 08:52:57	989.38
00088245002	2017-09-20 23:10:57	954.61
00088245003	2017-09-21 00:46:57	1014.18
00010264012	2017-09-22 15:15:57	1189.20
00010264013	2017-09-23 02:20:56	1009.60
00010264014	2017-09-24 02:25:57	599.20
00773893000	2017-09-24 09:54:14	620.93
00010264015	2017-09-25 21:28:56	899.48
00010264016	2017-09-26 18:12:56	909.21
00010264017	2017-09-27 16:37:57	859.22
00010264018	2017-09-28 18:01:57	1044.60
00010264019	2017-09-29 17:56:57	964.65
00010264020	2017-09-30 17:56:57	889.61
00010264021	2017-10-01 17:46:56	874.61
00010264022	2017-10-02 17:44:56	1109.60
00010264023	2017-10-03 17:44:22	1004.60
00010264024	2017-10-04 17:40:57	964.60
00010264025	2017-10-05 15:53:27	604.61
00010264026	2017-10-06 11:06:57	1154.60
00010264027	2017-10-07 04:35:57	1024.60
00010264028	2017-10-08 05:53:56	974.60
00010264029	2017-10-09 10:51:57	1059.61
00010264030	2017-10-10 12:03:57	994.06
00010264031	2017-10-11 07:32:57	854.62
00088245004	2017-10-22 23:40:57	2088.03
00088246001	2017-10-24 23:28:57	1528.19
00010490007	2017-12-31 06:36:57	109.75
00010491001	2017-12-31 06:39:31	869.95
00010492001	2017-12-31 06:41:06	864.96
00010493001	2017-12-31 06:42:39	915.76
00010494001	2017-12-31 06:44:12	877.77
00010495001	2017-12-31 06:45:41	885.02
00010496001	2017-12-31 06:47:05	724.70
00010497001	2017-12-31 06:48:28	847.41
00010491002	2018-01-19 08:05:57	1119.61
00010264032	2018-03-17 19:13:28	279.61
00010264033	2018-03-18 10:47:57	1370.34
00010264034	2018-03-24 21:16:57	1859.22
00010264035	2018-03-26 13:28:47	1409.22
00010264036	2018-03-28 13:23:57	2015.28
00010264037	2018-03-30 02:03:57	1910.27

This paper has been typeset from a TEX/LATEX file prepared by the author.